Development of MRI-based Axillary Numerical Models and Estimation of Axillary Lymph Nodes Dielectric Properties for Microwave Imaging

Daniela M. Godinho[1], João M. Felício[2,3], Tiago Castela[4], Nuno A. Silva[5], M. Lurdes Orvalho[4], Carlos A. Fernandes[3], and Raquel C. Conceição[1]

[1] Instituto de Biofísica e Engenharia Biomédica, Faculdade de Ciências da Universidade de Lisboa, 1749-016 Lisbon, Portugal

[2] Centro de Investigação Naval (CINAV), Escola Naval, 2810-001 Almada, Portugal

[3] Instituto de Telecomunicações, Instituto Superior Técnico, Universidade de Lisboa, 1049-001 Lisbon, Portugal

[4] Departamento de Radiologia, Hospital da Luz Lisboa, Luz Saúde, 1500-650 Lisbon, Portugal

[5] Hospital da Luz Learning Health, Luz Saúde, 1500-650 Lisbon, Portugal

Version typeset July 28, 2021

Corresponding author: Daniela M. Godinho. email: dgodinho94@gmail.com

Abstract

Purpose: Microwave Imaging (MWI) has been studied as a complementary imaging modality to improve sensitivity and specificity of diagnosis of Axillary Lymph Nodes (ALNs), which can be metastasised by breast cancer. The feasibility of such a system is based on the dielectric contrast between healthy and metastasised ALNs. However, reliable information such as anatomically realistic numerical models and matching dielectric properties of the axillary region and ALNs, which are crucial to develop MWI systems, are still limited in the literature. The purpose of this work is to develop a methodology to infer dielectric properties of structures from Magnetic Resonance Imaging (MRI) images, in particular, ALNs. We further use this methodology, which is tailored for structures farther away from MR coils, to create MRI-based numerical models of the axillary region and share them with the scientific community, through an open-access repository.

Methods: We use a dataset of breast MRI scans of 40 patients, 15 of them with metastasised ALNs. We apply image processing techniques to minimise the artefacts in MR images and segment the tissues of interest. The background, lung cavity, and skin are segmented using thresholding techniques and the remaining tissues are segmented using a K-Means clustering algorithm. The ALNs are segmented combining the clustering results of two MRI sequences. The performance of this methodology was evaluated using qualitative criteria. We then apply a piecewise linear interpolation between voxel signal intensities and known dielectric properties, which allow us to

i

create dielectric properties maps within a MRI and consequently infer ALNs properties. Finally, we compare healthy and metastasised ALNs dielectric properties within and between patients, and we create an open-access repository of numerical axillary region numerical models which can be used for electromagnetic simulations.

Results: The proposed methodology allowed creating anatomically realistic models of the axillary region, segmenting 80 ALNs and analysing the corresponding dielectric properties. The estimated relative permittivity of those ALNs ranged from 16.6 to 49.3 at 5 GHz. We observe there is a high variability of dielectric properties of ALNs, which can be mainly related to the ALN size and, consequently, its composition. We verified an average dielectric contrast of 29% between healthy and metastasised ALNs. Our repository comprises 10 numerical models of the axillary region, from 5 patients, with variable number of metastasised ALNs and Body Mass Index.

Conclusions: The observed contrast between healthy and metastasised ALNs is a good indicator for the feasibility of a MWI system aiming to diagnose ALNs. This paper presents new contributions regarding anatomical modelling and dielectric properties characterisation, in particular for axillary region applications.

I. Introduction

More than 0.5 million women per year have lymph nodes, such as the Axillary Lymph Nodes (ALNs), affected due to breast cancer metastasis[1,2].

The number of metastasised ALNs is one of the factors considered for breast cancer staging and therefore affects treatment decisions[3]. Currently, in a first stage, ALNs diagnosis is performed using medical imaging techniques, such as Magnetic Resonance Imaging (MRI) and Ultrasound. However, sensitivity and specificity of imaging modalities are still unsatisfactory, with a large range of 20%-90% and 40%-96%, respectively[4,5]. Biopsy is still the most accurate technique to identify metastasised ALNs, with 100% specificity and around 90% sensitivity[6,7], but it is an invasive and time-consuming procedure. Therefore, there is a need for alternative imaging modalities, and Microwave Imaging (MWI) may be one alternative. MWI is a low-cost, low-power and non-invasive technique which has already yielded promising results for early breast cancer diagnosis[8] and brain stroke detection[9]. MWI has been recently studied to work as a complementary diagnostic tool to detect metastasised ALNs[10,11,12].

Anatomically realistic models of the region of interest are crucial to accurately develop and validate MWI systems, and axillary region numerical models with these characteristics do not exist in the literature. Our group has presented two physical axillary region models[11,12], one of them with realistic representations of muscle, lung and bone. However, the ALNs included in the models were an approximation of true ALN shapes and their positioning. Other models such as Virtual Population models[13] also have limitations for MWI use, mainly because the positioning of the arm does not allow the use of a MWI device, which should have direct access to the axillary region. Also, these models do not detail the variability of ALN shapes and pathology status. Information regarding tissue dielectric properties and the dielectric contrast between tissues is also important when developing numerical or physical models. An international effort is under way to gather this type of information which is useful for the development of both electromagnetic diagnostic and therapeutic devices[14]. From a diagnostic point-of-view, a real representation of the dielectric behaviour is important to validate whether MWI algorithms are able to reconstruct images with identifiable targets in a clinical scenario[15]. At microwave frequencies, the most relevant dielectric properties are the relative permittivity (ϵ_r) and conductivity (σ), which mostly depend on water content

of tissues. Cancerous tissues have reportedly higher properties than healthy tissues due to increased vascularization[16]. The dielectric properties of tissues such as skin, bone, muscle and breast (fibroglandular and adipose) have been widely studied[17,18]. Nonetheless, the information regarding dielectric properties of ALNs is still limited.

A few studies carried dielectric properties measurements of ALNs using the Open-Ended Coaxial-Probe (OECP) method[11,16,19,20], both in animal and human ALNs. However, usually human ALNs samples have to remain intact due to clinical constraints and only their surface is measured. In general, the authors observed the complex permittivity results extracted from the measurements on the external surfaces are dominated by the fat layer surrounding the ALNs at the time of excision, resulting in lower permittivity and conductivity. A large variability of dielectric property values was observed in all measurements (5 to 55 at 4 GHz[11,20]). More recently, Yu *et al.*[21] measured human intrathoracic LNs removed from lung cancer surgeries and verified metastasised LNs presented significantly higher dielectric properties than healthy LNs. However, the studied frequency range (1 MHz to 4 GHz) does not cover the entire frequency range of interest for MWI applications (typically comprised in the 0.5 to 10 GHz range), and the cancer and LNs in the thorax region may not be comparable with ALNs metastasised by breast cancer.

Although these studies have presented relevant information to establish ALNs dielectric properties, there are some points that need to be further explored. Firstly, the heterogeneity of ALNs samples needs to be considered. As reported by the mentioned studies, ALNs are usually covered by a fat layer which hampers the results of the real dielectric properties of ALNs. Additionally, one also needs to consider that ALNs are heterogeneous organs. In fact, ALNs are composed by a capsule of collagen fibres and divided into lymphoid follicles, where the lymphocytes and macrophages are located. In the centre of the node there is a region called the hilum where the efferent lymphatic vessel carrying the lymph out of the node is connected[22]. The hilum is a fatty region, in contrast to the remaining ALN composition. These two aspects of the ALN composition can hamper OECP results, as this technique has known limitations associated to measuring heterogeneous structures[23]. Secondly, only a very limited number of metastasised ALNs was measured, which ranged from 1 to 12 metastasised ALNs in each study[16,19,20]. Those numbers are not sufficient to infer a dielectric contrast between healthy and metastasised ALNs with confidence, which would have been important to evaluate the feasibility of distinguishing these structures at microwave frequencies.

In this paper, we use MRI scans for two purposes: (i) the creation of numerical anatomically-realistic models of the axillary region with both healthy and metastasised ALNs; (ii) and estimation of dielectric properties of heterogeneous structures (e.g. ALNs) from MR images, which are difficult to measure with traditional techniques. We recently presented a brief description of our preliminary methodology and results of the estimation of ALN dielectric properties with only one patient[24]. In this paper, we present our improved methodology, which uses state-of-the-art dielectric properties information of other structures to infer ALN properties and validate it in a larger database of patients' MRIs with both healthy and metastasised ALNs. We also present an open-access repository of axillary region numerical models, which can be used for electromagnetic simulations, and, we believe, is an important contribution to the community. Other authors have presented comparable methodologies regarding the creation of MRI-based numerical models, in particular for breast models[25,26,27,28]. However, structures of the torso which are more challenging to segment were not included in such models. Also, lymph nodes segmentation was only addressed in studies where the purpose was to detect and isolate them from other tissues[29,30,31]. The estimation of dielectric properties from MRI were not addressed by these studies. To that end, only MR-based Electrical Properties Tomography has been studied[32,33], however this method is limited to the Larmor's frequency (up to 300 MHz), which is low compared to the frequency range of interest for MWI. Our study is the first one using common MRI sequences data to infer unknown dielectric properties based on state-of-the-art properties, which can be used independently of the frequency of MRI acquisition. Although there is an inherent uncertainty in the estimated values, since MR images are not quantitative, and these values cannot be considered as absolute, a comparison between the observations is possible. This methodology can also be extended to other parts of the body which are not well-covered by dedicated MRI coils.

In section II, we present the details of the MRI dataset used in this study and the methodology of the pre-processing pipeline and segmentation. In section III, we present the step-by-step results of our proposed methodology, the results of ALN dielectric properties estimation and the details regarding the open-access repository of axillary region numerical models. In section IV, we discuss the obtained results, and finally, in section V, we present the main conclusions of this study.

II.   Materials and Methods

In the following sections we present the MRI dataset used for this study, an analysis of the tissues of interest of the axillary region, and the image processing pipeline.

II.A.   Dataset

Our dataset includes breast MRI exams from 40 female patients acquired with a 3.0T clinical MR system (Magnetom Vida, Siemens Healthineers) with an 18-channel dedicated breast coil, at Hospital da Luz Lisboa, during regular breast cancer screenings or follow-ups. This study was approved by the Scientific and Ethical Commission, under references CES/44/2019/ME and CES/34/2020/ME, and an informed consent was obtained from all patients. Only exams from patients with visible lymph nodes were included in the study. The patients are divided in two groups, patients with only healthy ALNs and patients with one or more metastasised ALNs. The demographic patient data is shown in Table 1.

Following the clinical protocol, we use three different MRI sequences of the breast and upper torso: 1) Direct transversal three-dimensional (3D) T1-weighted (T1-w) Fast Low Angle Shot 3D (fl3D) Volumetric Interpolated Breath-hold Examination (VIBE) localisation image sequence; 2) Direct coronal two-dimensional (2D) T2-weighted (T2-w) Turbo Spin Echo (TSE) with short-time inversion recovery pulse (STIR) image sequence; and 3) Direct axial isotropic 3D T1-w fl3D VIBE Dixon image sequence (T1-w Dixon).

The T1-w localisation image sequence is used to retrieve the overall shape of the axillary region and all contours of the upper torso. Due to its low acquisition time (approximately

Table 1: Demographic data of the database of patients.

	Healthy ALNs (n=25)			Metastasised ALNs (n=15)		
	Mean	SD	Range	Mean	SD	Range
Age	50	10	34 to 73	56	14	39 to 81
BMI	28	6	17 to 44	28	5	20 to 36

BMI: Body Mass Index; SD: Standard Deviation.

169 9 seconds), we obtain this information avoiding a substantial increase of the duration of the

170 MRI exam, at the expense of lower signal-to-noise ratio. The voxel size is $0.86 \times 0.86 \times$

171 1.8 mm^3 and, although it is not isotropic, it has enough resolution to allow for Multiplanar

172 Reconstruction (MPR) at sagittal and coronal views, for a complete anatomical evaluation.

173   The 2D T2-w STIR is acquired in the coronal plane and is the most used sequence by

174 radiologists to detect ALNs, since ALNs are usually very well-defined in images reconstructed

175 with this sequence. However, such image sequence has an overall spatial resolution of $4 \times$

176 0.75×0.75 mm^3, resulting in low resolution in the transversal and sagittal planes, meaning

177 an additional sequence must be used.

178   The T1-w Dixon image sequence provides good contrast between internal tissues, such

179 as muscle, adipose and fibroglandular tissues. The image is acquired in the coronal plane

180 but the voxels are isotropic $(0.99 \times 0.99 \times 1 \text{ mm}^3)$, allowing an MPR in all anatomical planes

181 without major image artefacts. This image sequence provides four image sets with different

182 contrasts. For the purpose of this study, we use the Water (W) and Fat (F) image contrasts.

183 T1-w Dixon-W voxel signal intensities correspond directly to the amount of Hydrogen nuclei

184 present in tissues, not only in free water. Nonetheless, in general, we can assume higher

185 water content tissues are represented with higher signal intensity values in T1-w Dixon-W.

186 Although MRI is not quantitative, a relationship between voxel signal intensities and water

187 content (and consequently dielectric properties) can be assumed. However, this assumption

188 needs to be carefully confirmed for each tissue type individually.

189   In these MR images, 8 main type of tissues are imaged: adipose tissue, fibroglandular

190 tissue, skin, lungs, muscles, bones, costal cartilage, and, finally, ALNs. Table 2 shows

191 the relationship between signal intensities on T1-w Dixon-W, water content and reported

192 dielectric properties of each tissue at 5 GHz. The water content of the lung is not shown

193 since there are several factors affecting the water content measurement and the water content

194 of the lung is usually reported depending on its individual structures[34], which includes air,

195 parenchyma and blood vessels. The accuracy of the voxel signal intensities is affected by

196 the large distance to the coil which is not tailored to image the lung and its different sub-

197 structures are not detected. Therefore, the relationship between voxel signal intensities,

198 water content and dielectric properties cannot be easily inferred.

199   Regarding the remaining tissues (namely: adipose, bone, fibroglandular, muscle, skin

Table 2: Tissue analysis by qualitative signal intensity of T1-w Dixon-W images, water content and dielectric properties (at 5 GHz).

Tissue	Qualitative signal intensity	Water content (%)	ϵ_r	σ (S/m)
Adipose	Dark	6-36[42]	3.8-7.0[18]	0.1-0.4[18]
Lung	Dark	-	19.0[17]	1.7[17]
Bone	Dark Gray	12-40[34,42]	10.0[17]	1.0[17]
Fibroglandular	Dark/Light Gray	30-73[34]	33.7-48.5[18]	2.7-4.7[18]
Muscle	Light Gray	70-79[42,43]	49.5[17]	4.0[17]
Skin	Light Gray	58-72[34,42]	35.8[17]	3.1[17]
Costal cartilage	Bright	60-75[34,44]	33.6[17]	4.1[17]

and costal cartilage), only skin and costal cartilage show different relationships between water content, dielectric properties and qualitative signal intensity. Skin presents similar signal intensities to muscle but has lower water content (and permittivity) when compared to muscle. This is explained by skin proximity to the coil placed around the breast, which inherently results in higher signal intensity values. Costal cartilage, in particular, is mainly composed by water and collagen which, due to its high number of Hydrogen atoms, results in increased signal intensities in T1-w Dixon-W images. However, this tissue is not relevant for the imaging of the axillary region and we can assume a direct relationship between dielectric properties, water content and signal intensity values for the remaining tissues.

II.A.1. Axillary Region Features

For the axillary region, skin, adipose tissue, ALNs and muscle are the most relevant tissues. In this region, bones and muscles are indistinguishable and the MRI contrast between them is very low so it is not possible to segment them separately. For the purpose of MWI, this does not pose a problem since the location of muscle in the axillary region is shallower than bone, and therefore bone MWI response will be much lower than muscle.

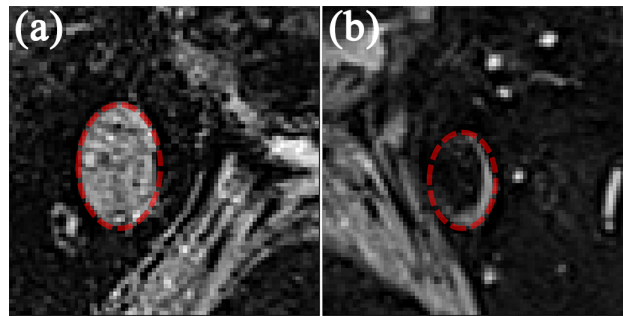Fig. 1 shows examples of a metastasised and a healthy ALNs in T1-w Dixon-W images.

Figure 1: Partial coronal slices with (a) a metastasised and (b) a healthy ALN marked with a red dashed ellipse.

The larger axis of both ALNs is around 2 cm. The healthy ALN has a large hilum represented by dark signal intensities inside the marked red dashed ellipse. The thin semi-ellipse contour corresponds to the cortex and the remaining structures of the ALN. The metastasised ALN has no hilum and most of the structure is represented by light gray signal intensities.

Fig. 2 presents a simplified flowchart of the main steps of our methodology, which is described in the following sections.

II.B. Image pre-processing pipeline

In this sub-section we describe the image pre-processing pipeline, which should be applied to ensure a correct segmentation of tissues.
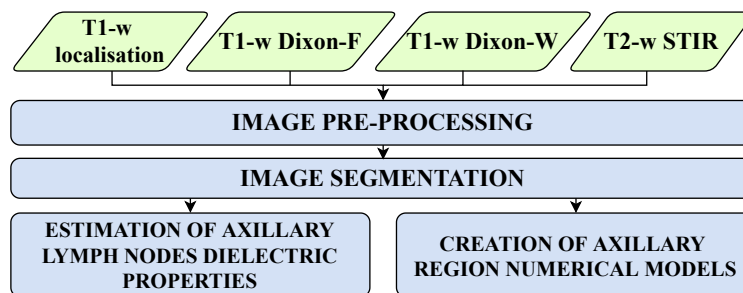
Figure 2: Simplified flowchart of the main steps of our methodology.

II.B.1.   Image registration

T1-w localisation, T2-w STIR and T1-w Dixon image sequences have different spatial resolutions and dimensions. In order to be able to correctly superimpose them, they need to be spatially registered to the same spatial reference system.

We use the ITK's implementation[35] of an affine registration with linear interpolation to register both T1-w localisation and T2-w STIR (moving images) to T1-w Dixon (static image). This combination of moving and static images is chosen since the latter has higher resolution and includes the more important information. The resulting images are transformed to the same referential system and have the same dimensions and resolution of the static image. In order to preserve the information in T1-w localisation image, before applying the registration algorithm, we increase the image size of T1-w Dixon without changing its resolution.

II.B.2.   Bias field removal

The bias field is an artefact produced during the MRI acquisition due to the magnetic field, the patient and coil positions, which creates an unrealistic variation of signal intensities within the tissues of the same type. This effect increases on the body parts that are farther away from the coil and when the body is not symmetrically positioned relative to the coil. In images of patients with higher Body Mass Index (BMI) this effect is even more evident. The T1-w Dixon sequence was chosen due to the reduced effect of bias field on this type of images, however it still needs to be removed. This step is essential for the remaining pipeline for two reasons:

1. Improve segmentation: Most of segmentation algorithms are highly dependent on voxel signal intensities. Thus, the voxel signal intensities within each tissue should be similar in order to be correctly segmented.

2. Ensure ALN dielectric properties reliability: The voxel signal intensities of all tissues will be important to infer ALN dielectric properties. Also, in order to compare different ALNs from both axillary regions, tissues with the same composition in both sides of the body should be equally represented in MR images.

253 Other authors use point-by-point bias field removal[26] but this is not viable for such a large
254 volume which includes both the breast and axillary regions. N4 (improved non-parametric
255 non-uniform signal intensity normalisation) bias field removal has also shown promising
256 results in removing bias field from breast MR images[28]. We apply ITK implementation[36]
257 of N4 bias field removal to T1-w localisation image and T1-w Dixon image sequences. The
258 algorithm receives as input both the original image and the negative binary mask of adipose
259 tissue obtained from an Otsu's thresholding of the original image. Otsu's method finds the
260 optimal threshold through an iteration process where the intra-class variance is minimised.

II.B.3. Selection of region of interest

262 We select a region of interest on each image in order to avoid including regions of the body
263 with little interest to the purpose of MWI which could compromise the performance of the
264 algorithms. The selection of a region of interest is optional but an improvement of the results
265 is observed when the selection is applied.

266 T1-w localisation and T1-w Dixon-W image sequences should contain both breasts and
267 axillary regions, while only the axillary region needs to be included in the T2-w image.

II.B.4. Filters and Normalisation

269 We apply a median filter to remove noise and to smooth the voxel signal intensity differences
270 within each tissue, for both T1-w Dixon-W and T2-w STIR image sequences. A more
271 powerful filter needs to be used for T1-w localisation image sequence, so we use a gaussian
272 filter with $\sigma = 1$.

273 Then, we apply a minimum-maximum normalisation to the voxel signal intensities of
274 each image, which is important for step III.B.. The normalisation does not have an impact
275 on the quality of the images.

II.C.   Image segmentation

277 We apply five segmentations methods to the breast MR images, which are described in the
278 following sub-sections. Fig. 3 summarises the steps of image segmentation, which comprises
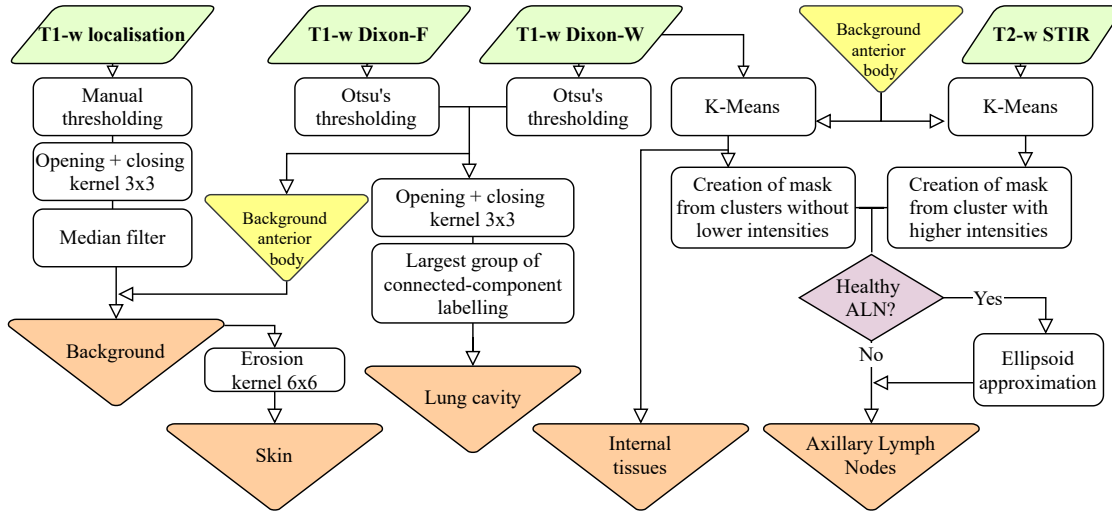279 a novel methodology for ALN segmentation.

Figure 3: Simplified flowchart of the image segmentation steps. Orange triangles represent the final segmentation masks.

II.C.1. Background

Contrary to previous studies[25,26,27] where only the breast region was segmented, for the axillary region we also need to retrieve the lateral and posterior part of the body. Therefore, the background is segmented in two steps. Firstly, we segment the background of the anterior part of the body using both T1-w Dixon-W and T1-w Dixon-F image sequences, due to their high signal-to-noise ratio. The background is segmented from the binarisation of both images using Otsu's thresholding[37] and applying the union of both resulting binarised images (masks). Then, each axial slice of the resulting mask is scanned from the anterior to the posterior part, filling the empty space. The background mask is used to select the body on the T1-w Dixon-W to improve the results of the next segmentation step by removing artefacts.

Finally, we generate the background of the posterior part of the body so this part of the body can be included in the axillary region models. This background is obtained using the T1-w localisation image sequence since it is the only sequence which contains the posterior part of the body. The background is segmented by applying a manual thresholding, followed by opening and closing operations with a kernel 3×3 and a median filter. Then, both backgrounds of the anterior and posterior part of the body are combined. The final background can have some unexpected errors which can be corrected by using manual segmentation and

298 by applying a univariate smoothing spline in the sagittal plane.

II.C.2.   Internal tissues

300 The internal tissues are segmented by applying the K-Means algorithm. This algorithm sep-
301 arates the tissues into K clusters according to their signal intensities values[38]. We compare
302 several values of K, from 3 to 10, and the best value is empirically found considering some
303 qualitative criteria.

304 The following criteria are followed for T1-w Dixon-W images: 1) There is a good dis-
305 tinction between the following tissues: fibroglandular tissue, adipose tissue, and muscle; 2)
306 Lymph nodes can be identified in more than one cluster but need to be isolated from the
307 surrounding tissues; and 3) One single main tissue cannot be identified in more than three
308 clusters. We use the same algorithm with T2-w STIR image sequence. There is only a
309 difference regarding the chosen criteria: the criterion is that ALNs need to be segmented in
310 one cluster.

II.C.3.   Lung cavity

312 The lung cavity is usually segmented in the same cluster as adipose tissue, so an additional
313 step is needed to segment this part of the torso. Even though this structure might have
314 minimal importance to MWI applications since it is deep and located behind the axillary
315 region muscles, it is included in the axillary region models to ensure a realistic anatomical
316 representation.

317 The segmentation of the lung cavity results from the intersection between the binarisa-
318 tion using Otsu's thresholding of both T1-w Dixon-W and T1-w Dixon-F image sequences.
319 The resulting mask includes some voxel groups which do not belong to the lung cavity.
320 Hence, we use opening and closing operations with a kernel 3×3 and apply a connected-
321 component labelling method which assigns different labels to each group of connected voxels
322 within the lung cavity mask. Then, we select the largest group which will indeed correspond
323 to the lung cavity.

II.C.4. Skin

The skin is often segmented in the same cluster as fibroglandular tissue or in more than one cluster, so an additional step is also needed to segment the skin. The algorithm consists in applying an erosion operation to each axial slice of the background mask. The kernel size is defined as twice the ideal skin thickness. For most cases, a kernel size of 6×6 is sufficient. The skin layer is obtained from the subtraction between the background mask and the resulting image after the erosion operation.

II.C.5. Axillary Lymph Nodes

Ideally, ALNs would be segmented with K-Means as only one tissue. But this is not always possible without compromising the segmentation of other tissues. Previous studies of breast or torso segmentation[25,26,27,28] have not included ALNs. Other studies[29,30,31] have addressed ALN segmentation but surrounding tissues were not segmented. The methods they presented are not appropriate for the purpose of our study, where a relationship between ALNs and the remaining tissues is needed. We segment ALNs by combining the resulting segmentations from K-Means of T1-w Dixon-W and T2-w STIR images. The ALNs mask is created from the intersection between the $K - 3$ highest-intensity clusters from T1-w Dixon-W segmentation and the highest-intensity cluster from T2-w STIR segmentation. As an example, if the best K value for T1-w Dixon-W segmentation is $K = 5$, the mask will be created considering the fourth and fifth clusters which correspond to tissues with higher signal intensities (ignoring adipose and intermediate tissues). For T2-w STIR segmentation, only the cluster with the highest signal intensities is selected, as it includes the ALNs. As explained in section II.A.1., only the ALN cortex has high signal intensities and is included in the segmentation. Finally, for each detected healthy ALN, we use the resulting segmentation to estimate an ellipsoid which includes the hilum.

The ellipsoid fitting method was adapted from an open-access code repository[39]. It applies a linear least squared algorithm[40] considering the algebraic form of an ellipsoid and a constraint: $Ax^2 + By^2 + Cz^2 + Dxy + Exz + Fyz + Gx + Hy + Iz + J = 0$ and $A + B + C = 3$.

After solving the equation system, we obtain the ellipsoid axes lengths (a, b and c), its center and orientation. These parameters are then used to create an ellipsoid mask in the

353 image which matches the true ALN shape.

II.D.   Estimation of Axillary Lymph Nodes Dielectric Properties

355 Fig. 4 summarises the process for estimation of ALN dielectric properties. We first assign
356 state-of-the-art dielectric properties of tissues (in particular, adipose and fibroglandular tis-
357 sues) to MRI-based numerical models. To this end, we consider a similar approach other
358 authors have used[25,26]. We consider six curves of dielectric properties (shown in Fig. 5) for
359 permittivity and conductivity of the tissues of interest based on the paper of Lazebnik *et*
360 *al.*[18,25]: two curves to limit both fibroglandular and adipose tissues, and one minimum and
361 one maximum curve, which correspond to the minimum and maximum limits of their mea-
362 surements, respectively. Nonetheless, as we are considering more than two tissues, we cannot
363 use a Gaussian fitting as suggested by other authors[25,26], and we tailored the methodology
364 to use our segmented results.

365 As shown in Fig. 6, each cluster obtained from the image segmentation is assigned
366 to an interval between two curves. At each frequency, the minimum and maximum voxel
367 signal intensities of each cluster are associated to the dielectric properties values of the
368 chosen curves (Fig. 6a). The voxel signal intensities are then mapped to a value between
369 the selected curves using a piecewise linear interpolation (Fig. 6b). If $K = 5$ in K-Means
370 algorithm, each original cluster is assigned to an interval between the curves. For lower
371 values of K, intermediate curves are neglected, while for higher values of K, clusters need to
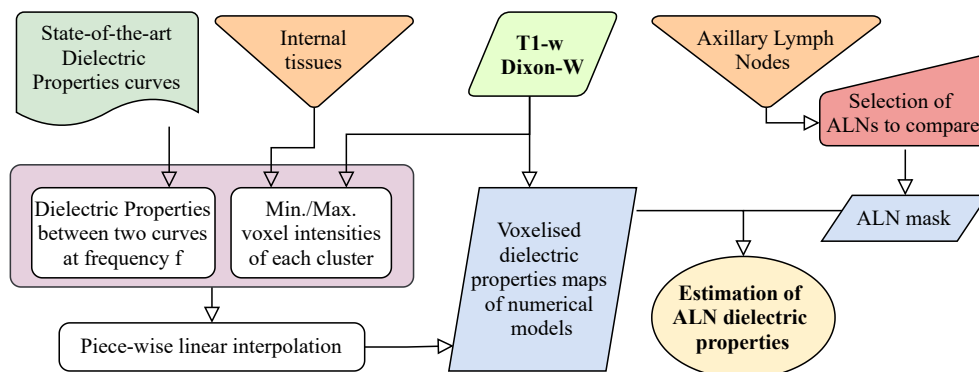

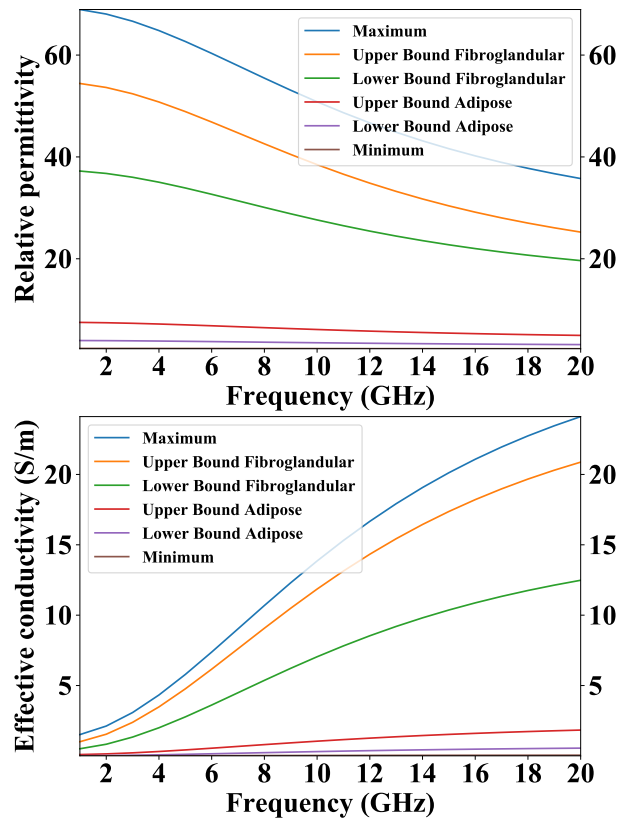Figure 4: Simplified flowchart of the steps for estimation of dielectric properties.

Figure 5: Relative permittivity (top) and conductivity (bottom) curves reported in the literature[18,25].

be grouped. Following this procedure, we can create voxelised dielectric properties maps (i.e. each voxel has the signal intensity value matching each dielectric property), for frequencies from 1 to 20 GHz, with a step of 1 GHz. This procedure also ensures the variation of water content within the tissues and between patients is observed through the variation of dielectric properties.

Finally, the properties of ALNs can be estimated by superimposing the ALNs mask with the resulting dielectric properties maps. For the purpose of this study, one ALN from each axillary region is selected for comparison. For patients with metastasised ALNs, one metastasised and one healthy ALNs are compared.

We apply a connected-component labelling method, which allows to select a specific ALN when the coordinates of a point of the ALN are given. The dielectric properties of an ALN for each frequency are obtained by averaging the assigned dielectric properties to each voxel. We calculate the first, second and third quartile curves for each group of healthy
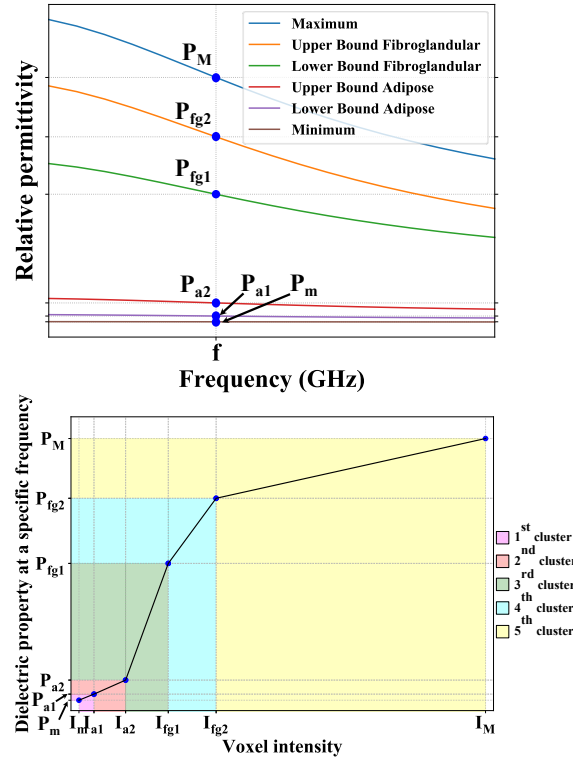
Figure 6: Interpolation between dielectric properties values and voxel signal intensities at a specific frequency f. Example of reference points of relative permittivity curves (top) and the piecewise linear interpolation considering 5 clusters (bottom).

and metastasised ALNs and we obtain the corresponding Debye parameters by fitting a Debye model using the non-linear least squares method. Finally, we apply a Mann-Whitney statistical test to evaluate the difference of dielectric properties between both groups of healthy and metastasised ALNs. A p-value ≤ 0.05 is considered as statistically significant.

II.E.   Creation of Axillary Region Numerical Models

The axillary region numerical models are created after adapting the segmented results from the image processing pipeline. In order to anatomically represent the tissues of interest, the obtained clusters from K-Means are grouped into two clusters: adipose and muscle/fibroglandular tissue. Multiple ALNs are included in the models after being selected following the connected-component labelling method described in section II.D. This method is also used to remove artefacts generated by vessel structures as it removes smaller subclusters within muscle/fibroglandular tissue cluster.

We then divide the model into two sections of each axillary region, using the nipples as the reference point for the limit in the sagittal direction and the bottom part of the breasts for the limit in the axial direction.

III. Results

In this section, we show some results of the image processing pipeline and the results from the estimation of ALN dielectric properties from MR images. Finally, we describe the content of the open-access repository.

III.A. Image pre-processing and segmentation

The following illustrative results are obtained from MR images of a patient with BMI of 26 (AR_004 model in the repository), who is considered overweight, and with metastasised ALNs on the right axillary region.

Fig. 7 shows the effect of applying a bias field removal algorithm for two axial slices, at the breast and at the axillary regions. In this particular case, the bias field affects more the internal region of the breast near the coil and the axillary regions are asymmetric. We observe the signal intensities are more homogeneous after applying the bias field removal. In particular, Fig. 7(d,h) shows the level of voxel intensities between the right and left side of the patient becomes similar after applying the bias field removal.

Fig. 8 shows the main steps of the background segmentation. Otsu's thresholding applied to both T1-w Dixon-W and T1-w Dixon-F result in complementary images which, when combined, generate a filled background mask. The T1-w localisation image has low contrast in the posterior part of the body but a mask can be generated using both manual thresholding and manual correction.

The segmentation results of the internal tissues using K-Means and the skin separate segmentation are shown in Fig. 9. We observe that usually muscle and part of fibroglandular tissue are segmented in the same cluster since they have similar range of voxel signal intensities. Nonetheless, they are visually distinguishable.

The segmentation results of the lung cavity are shown in Fig. 10, which show an
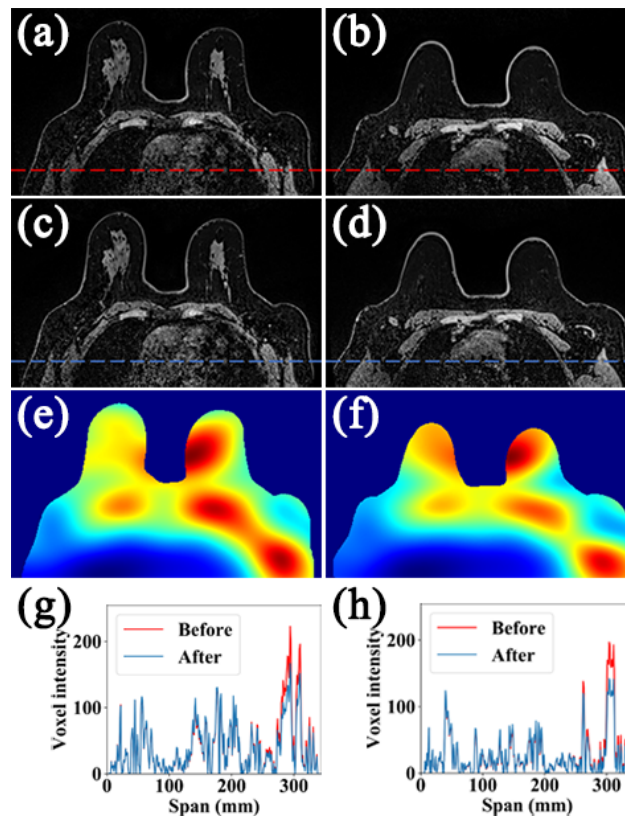
Figure 7: Bias field removal in inferior (left) and superior (right) axial slices of a breast MR image. The images show the slices (a,b) before and (c,d) after bias field removal is applied, (e,f) the computed bias field, and (g,h) voxel intensities variation over the line represented in (a,b). Blue and red colours in (g,h) represent a smaller and larger inhomogeneity between voxel signal intensities, respectively.

acceptable segmentation.

Fig. 11 shows the step-by-step results of ALNs segmentation, which results from the intersection between T1-w Dixon-W and T2-w STIR. In the represented coronal slice, only one matted metastasised ALN is segmented but each slice can include multiple ALNs. The resulting image from the intersection represents a more accurate representation of the lymph node shape and size, due to the higher resolution of T1-w Dixon-W. In Fig. 12, we show an example of a healthy ALN and the result of the ellipsoid estimation used to include the ALN hilum in the segmented ALN.
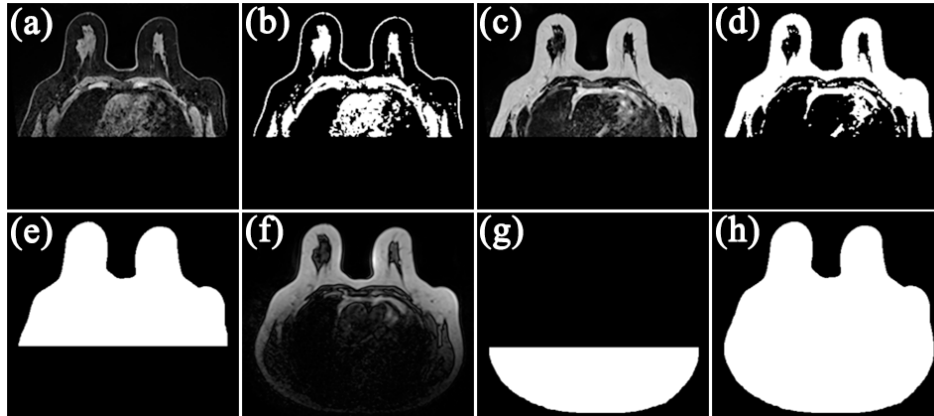
Figure 8: Background segmentation example of an axial slice of breast MR images. The images show (a) T1-w Dixon-W, (c) T1-w Dixon-F image sequences and the corresponding results of Otsu thresholding in (b) and (d), respectively. The combination and processing of both images (b, d) result in (e). T1-w localisation image is presented in (f) and the resulting image of the background segmentation is presented in (g). The final background is presented in (h).
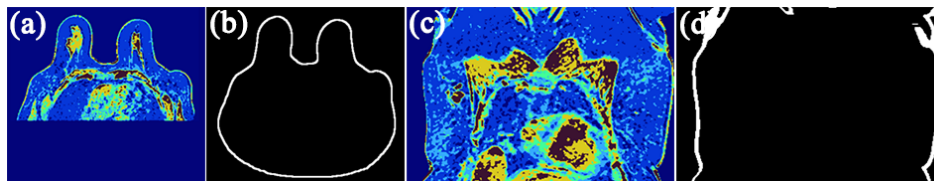

Figure 9: Slices of segmentation results in the (a,b) axial and (c,d) coronal planes. (a,c) shows the $K = 6$ clusters segmented by K-Means and (b,d) the skin segmentation obtained from the background mask.

III.B. Axillary Lymph Nodes Dielectric Properties

Our analysis resulted in estimating dielectric properties from 15 metastasised ALNs and 65 healthy ALNs (2 ALNs from each of the 25 patients with only healthy ALNs and 1 ALN from the 15 patients with metastasised ALNs). Fig. 13 shows the results of the estimated dielectric properties for each ALN over frequency. The first, second and third quartile curves for both healthy and metastasised ALNs are also showed in the same figure. We observe that healthy ALNs have a large variability of dielectric properties values, ranging from 16.6 to 41.1 of average relative permittivity at 5 GHz. The metastasised ALNs have higher dielectric properties and the variability is much lower than with the healthy ALNs, with
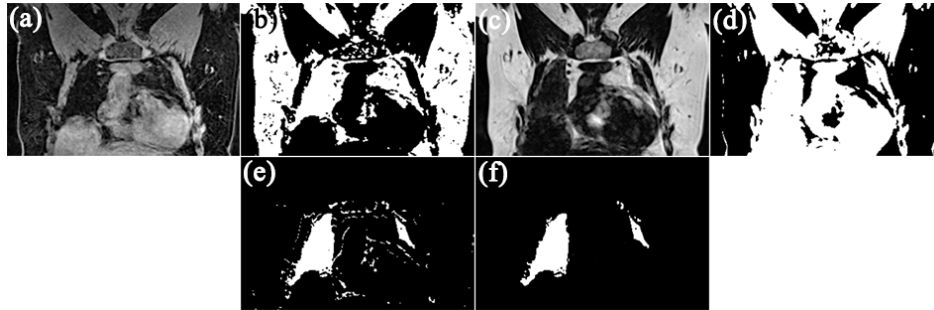
Figure 10: Coronal slices of lung cavity segmentation. The images show (a) T1-w Dixon-W, (c) T1-w Dixon-F image sequences and the corresponding results of Otsu thresholding in (b) and (d), respectively. (e) shows the resulting intersection between (b) and (d), and (f) the final result after the processing steps.
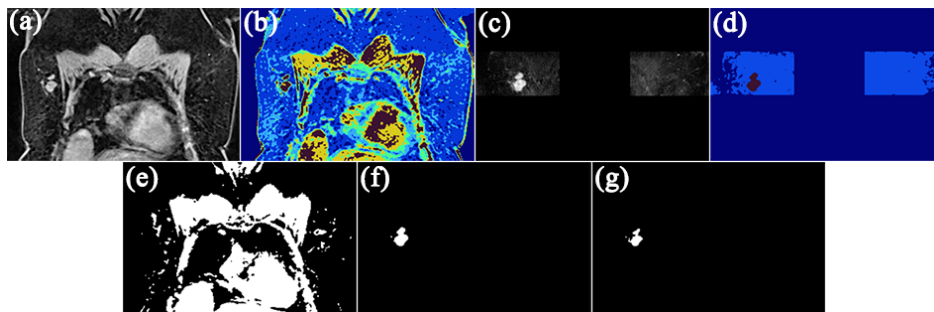

Figure 11: Coronal slices of segmentation of an axillary lymph node. The images show (a) T1-w Dixon-W, (c) T2-w STIR image sequences after selecting the region of interest and the corresponding K-means segmentation results in (b) and (d), respectively. The masks generated from (b) and (d) and their intersection are shown in (e), (f) and (g), respectively.

average relative permittivity ranging from 40.5 to 49.3 at 5 GHz. The estimated dielectric properties of healthy and metastasised ALNs are statistically different with a p-value of 10^{-9} for both relative permittivity and conductivity at 5 GHz. The contrast between the median of both healthy and metastasised groups is 29%. The parameters of the Debye model of the curves are presented in Table 3. The following analysis focus on relative permittivity values as they highlight absolute differences, but comparable conclusions can be drawn from conductivity results.

One of the factors that might explain the variability of permittivity values for healthy ALNs is the variability of their size. Fig. 14 shows how average relative permittivity values
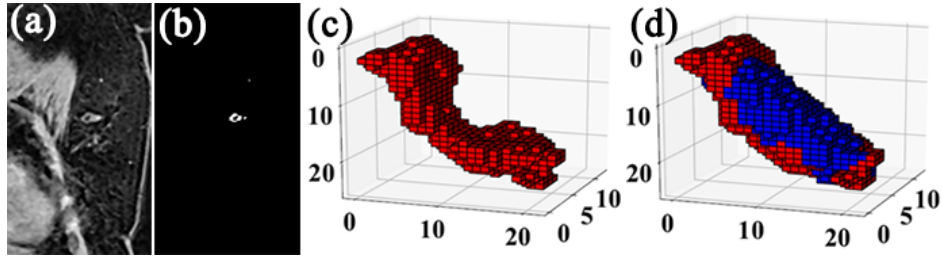
Figure 12: Ellipsoid estimation of a healthy Axillary Lymph Node (ALN). Coronal slice of original (a) T1-w Dixon-W image and (b) resulting mask. (c) 3D segmented volume and (d) resulting 3D volume from ellipsoid estimation. Voxels in red represent the ALN cortex and voxels in blue represent the hilum.
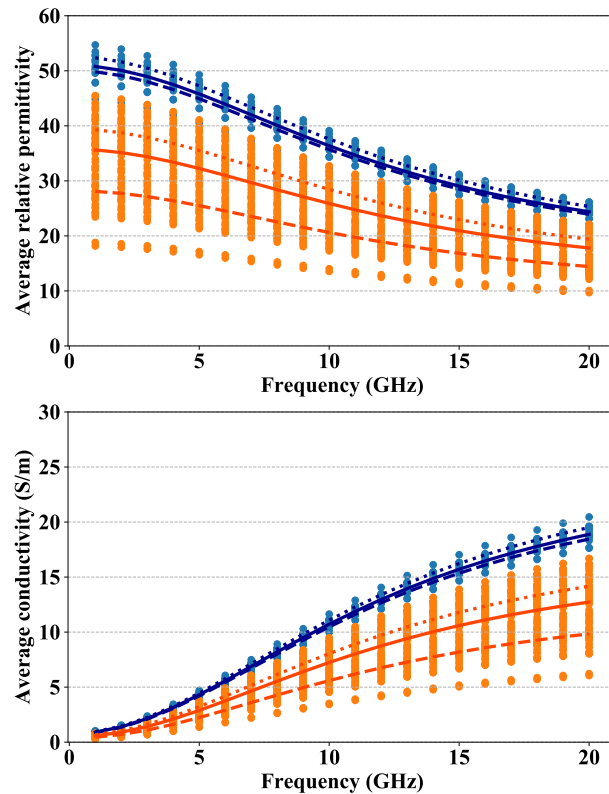

Figure 13: Relative permittivity (top) and conductivity (bottom) of healthy (orange) and metastasised (blue) Axillary Lymph Nodes (ALNs) estimated from MR images over frequency. The dashed, solid and dotted lines represent the first, second and third quartile of both healthy and metastasised ALNs, respectively.

change over the ALN larger axis length (i.e. the larger dimension of the ALN within the three image planes) or volume. We can observe a trend between relative permittivity and the

Table 3: Debye model parameters for healthy and metasta-
sised lymph nodes applied to 1 to 20 GHz frequency range.

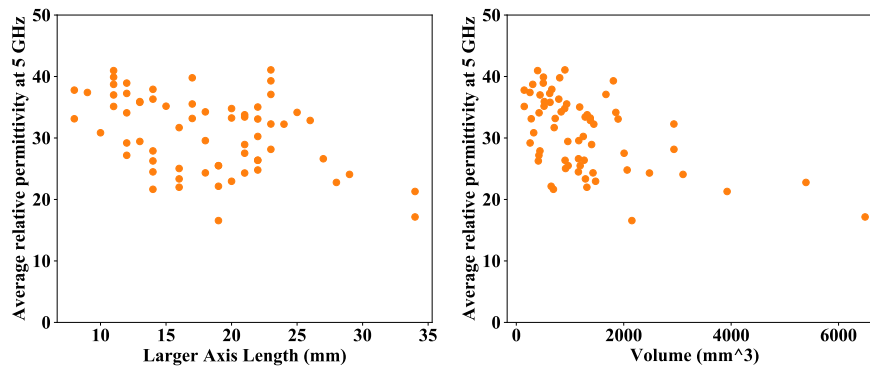|	Healthy ALNs			Metastasised ALNs		
Quartile	Q1	Q2	Q3	Q1	Q2	Q3
ϵ_∞	9.22	11.05	11.93	14.17	14.40	15.06
σ_s (S/m)	0.40	0.49	0.54	0.70	0.74	0.84
$\Delta\epsilon$	19.01	24.74	27.53	35.87	36.63	37.58
τ (ps)	13.00	13.00	13.00	13.00	13.00	13.00

Figure 14: Estimated relative permittivity at 5 GHz of each healthy
ALN over its larger axis length (left), and volume (right).

ALNs larger axis. However, this trend is more evident considering the total ALNs volume: smaller ALNs have higher relative permittivity values. This can be explained by the fact that smaller ALNs have a smaller hilum, hence the cortex is the ALN structure contributing more to the average dielectric properties of the ALNs.

We can evaluate the robustness of our methodology analysing patient-specific results. Fig. 15 shows a comparison between the resulting average relative permittivity values of ALNs within the same patient. The values vary between patients but they are all within a comparable range of values. This indicates that our methodology does not result in distinct intervals per patient or neither the same interval across patients. We can also observe that the relative permittivity contrast between healthy and metastasised ALNs within the same patient is larger (on average 33%) than between healthy ALNs (on average 16%).
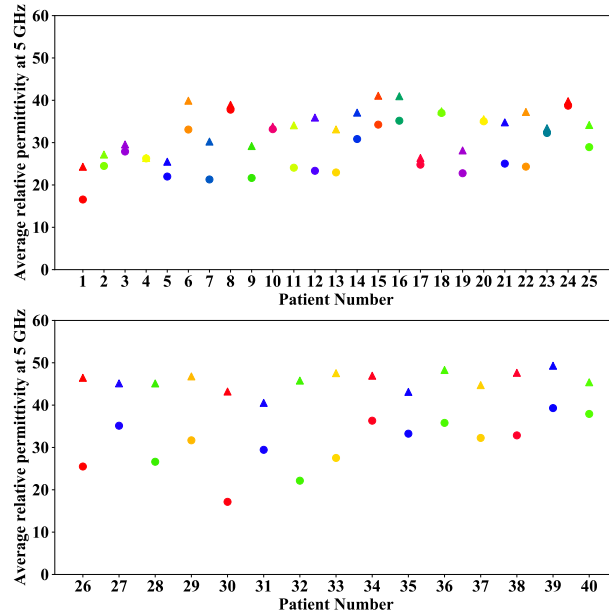
Figure 15: Comparison of estimated relative permittivity within each patient for 5 GHz. Comparison between healthy ALNs (top) and between healthy and metastasised ALNs (bottom).
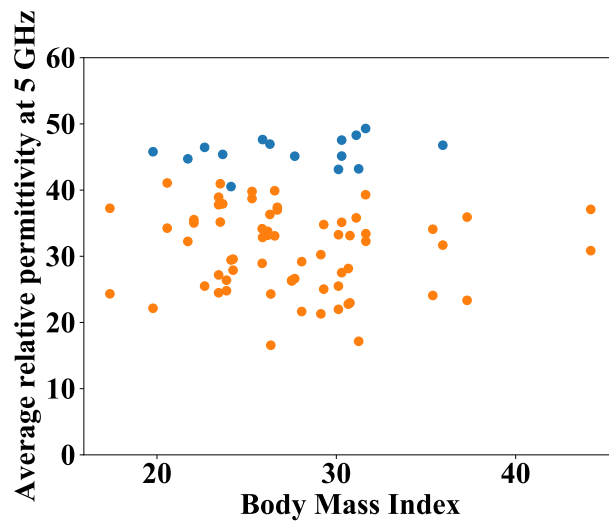

Figure 16: Estimated relative permittivity at 5 GHz of each ALN over the patient's BMI. Healthy ALNs are represented in orange and metastasised ALNs in blue.

Fig. 16 shows the relative permittivity change over the patients' BMI. BMI could have an impact on bias field and its removal performance which would result in changes of voxel signal intensities and, consequently, in estimated dielectric properties. We observe

that average relative permittivity values change independently of BMI, for both healthy and metastasised ALNs, so our methodology is sufficiently robust for all patients' BMI.

III.C. Repository of Axillary Region Models

The repository is available for download on GitHub[41] and includes numerical models of 5 patients, in order to provide variability of number of metastasised ALNs and BMI, as shown in Table 4. Fig. 17 also shows three examples of our models in 3D.

Each patient folder includes two sub-folders with the corresponding left and right axillary region models. Each group of tissues is provided in a single file so the users can combine and create models with different levels of complexity. Each axillary region model includes a maximum of 6 tissue types: adipose tissue, muscle and partial fibroglandular tissue, skin, lung, healthy ALNs and metastasised ALNs.

All files are provided in MAT, RAW and STL formats. Two additional files for adipose

Table 4: Specifications of axillary region models.

Model	Patient BMI	Side	Dimensions			Resolution			# H ALNs	# M ALNs
			A	C	S	A	C	S		
AR_001	21	Right	190	298	121	0.9965	0.9965	1	1	2 + 1 Matted
		Left	190	298	126				3	0
AR_002	24	Right	204	297	144	0.9965	0.9965	1	0	6
		Left	204	297	105				4	0
AR_003	26	Right	169	325	114	1.0764	1.0764	1	3	0
		Left	169	325	111				1	1 Matted
AR_004	26	Right	213	360	144	0.9965	0.9965	1	1	2
		Left	213	360	154				3	0
AR_005	31	Right	217	443	169	0.9965	0.9965	1	1	1
		Left	217	443	138				2	0

BMI: Body Mass Index; ALNs: Axillary Lymph Nodes; A: Axial Direction;

C: Coronal Direction; S: Sagittal Direction; H: Healthy; M: Metastasised.
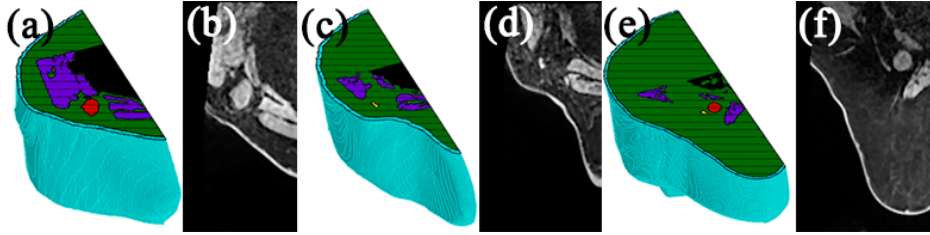
Figure 17: 3D representation with a 2D view and corresponding MR axial slice of (a,b) AR_001, (c,d) AR_003, and (e,f) AR_005 right axillary region models. Light blue colour represents the skin layer, green represents adipose tissue, purple represents muscle, black represents lung cavity, yellow represents a healthy lymph node, and red represents a metastasised lymph node.

and skin tissues without cavities are provided in STL format to allow the user to combine post-processing STL files. The models are numerical and no 3D-printing validation was performed. The dielectric properties can be assigned to the numerical models in two different ways. The first option consists in the implementation of the Debye models presented in Table 3 and the ones reported in literature for skin, lung, muscle and adipose tissue[17,18,25]. The second option consists of associating a dielectric property map for each frequency which is obtained from the interpolation between MRI voxel signal intensities and dielectric properties described in Section III.B.. For this option, we provide 2 additional files in MAT and RAW formats for each axillary region model and explain the calculation of the dielectric properties in the repository documentation.

IV. Discussion

Our image processing pipeline is partly inspired by other authors' work[25,26,27,28] but we designed new methodologies specifically for the axillary region application, such as the segmentation of ALNs. The differences between our methodology and the state-of-the-art methodologies are summarised in Table S-1. We also used this methodology with a new objective: estimate dielectric properties of structures for which dielectric property information is still limited. As mentioned in section I., the assumptions behind our methodology limit the direct comparison of absolute dielectric properties values with state-of-the-art values measured with traditional methods, such as OECP[11,20]. Also, a comparison with the patients included in our study is not possible since no follow-up of the patients was done.

Nonetheless, we can compare our results with the main conclusions drawn from those studies and highlight our contributions. The large range of the measured dielectric property values is common across studies. The range of the relative permittivity at 5 GHz we estimated from MRI was $16.6 - 49.3$ which is lower when compared to approximately $5 - 50$ measured with OECP. This happens because we impose minimum and maximum dielectric property curves obtained from measurements of breast tissues. Another reason lies on the fact that OECP measurements do not provide information on the heterogeneity of the samples, instead they provide a weighted average of the properties of the measured sensing volume of the ALN under measurement, and they may be hampered by the adipose layer covering the ALNs. Fig. 15 shows the variability of healthy ALNs within the same patient results in a contrast of 16% on average, which is lower than the verified contrast of 32% between healthy and metastasised ALNs. The contrast between the median values of healthy and metastasised ALNs of all patients is slightly lower (29%) (Fig. 13). This level of contrast is a good indicator for the feasibility of a MWI system aiming to diagnose ALNs.

The axillary region models included in our repository were created from a selection of patients from a larger dataset of 40 patients, ensuring the representativeness of axillary regions with both healthy and metastasised ALNs (Table 4). When presenting numerical models of patients with different BMIs, we are ensuring variability of ALNs depth and positioning relatively to the surrounding muscles. Different types of metastasised ALNs are also represented, such as single ALNs, multiple clearly separated ALNs or matted ALNs. The numerical models have the original resolution of the MRI scans, so users might need to use post-processing steps such as interpolation or smoothing filters to fit the electromagnetic simulation software requirements. This repository is an important contribution to the community and is a useful tool for the development and validation of dedicated algorithms for MWI systems aiming to diagnose ALNs.

V. Conclusions

We proposed a methodology to create MRI-based numerical models of body regions which are farther away from the MRI coil and to infer dielectric properties of biological tissues which are not well-reported in the literature. With this methodology, we performed a study of dielectric properties of both healthy and metastasised ALNs estimated from MR images and

created an open-access repository of anatomically realistic numerical models of the axillary region for electromagnetic applications. The methodology included novel steps towards the segmentation of ALNs and estimation of their dielectric properties. The results showed there is a 29% contrast between healthy and metastasised ALNs, which is a good indicator to pursue the development of ALN-MWI systems.

In future work, we intend to use our models and their dielectric properties to validate a MWI system to diagnose ALNs.

Data Availability Statement

The data that support the findings of this study are openly available in "Axillary Region Models Repository for Electromagnetic Application" at https://github.com/dmgodinho/axillary-region-models-repository, reference number 44.

References

[1] The Global Cancer Observatory - World Health Organization, Breast Cancer Fact Sheets, Available online: http://gco.iarc.fr/today, 2020.

[2] C. E. DeSantis, J. Ma, A. Goding Sauer, L. A. Newman, and A. Jemal, Breast cancer statistics, 2017, racial disparity in mortality by state, CA: A Cancer Journal for Clinicians **67**, 439–448 (2017).

[3] American Joint Committee on Cancer, Breast Cancer, in *AJCC Cancer Staging Manual*, Springer, 8th ed. edition, 2018.

[4] R. George, Selective Application of Routine Preoperative Axillary Ultrasonography Reduces Costs for Invasive Breast Cancers, The Oncologist **16**, 1069–1069 (2011).

[5] S. A. Valente, G. M. Levine, M. J. Silverstein, J. A. Rayhanabad, J. G. Weng-Grumley, L. Ji, D. R. Holmes, R. Sposto, and S. F. Sener, Accuracy of predicting axillary lymph node positivity by physical examination, mammography, ultrasonography, and magnetic resonance imaging, Annals of Surgical Oncology **19**, 1825–1830 (2012).

[6] U. Veronesi, G. Paganelli, G. Viale, A. Luini, S. Zurrida, V. Galimberti, M. Intra, P. Veronesi, C. Robertson, P. Maisonneuve, G. Renne, C. De Cicco, F. De Lucia, and

R. Gennari, A randomized comparison of sentinel-node biopsy with routine axillary dissection in breast cancer, New England Journal of Medicine **349**, 546–553 (2003).

7 D. N. Krag, S. J. Anderson, T. B. Julian, A. M. Brown, S. P. Harlow, T. Ashikaga, D. L. Weaver, B. J. Miller, L. M. Jalovec, T. G. Frazier, R. D. Noyes, A. Robidoux, H. M. C. Scarth, D. M. Mammolito, D. R. Mccready, and P. Eleftherios, Technical outcomes of sentinel-lymph-node resection and conventional axillary-lymph-node dissection in patients with clinically node-negative breast cancer : results from the NSABP B-32 randomised phase III trial, The Lancet Oncology **8**, 881–888 (2007).

8 M. Shere, I. Lyburn, R. Sidebottom, H. Massey, C. Gillett, and L. Jones, MARIA ® M5: A multicentre clinical study to evaluate the ability of the Micrima radio-wave radar breast imaging system (MARIA ®) to detect lesions in the symptomatic breast, European Journal of Radiology **116**, 61–67 (2019).

9 J. A. Vasquez, R. Scapaticci, G. Turvani, G. Bellizzi, D. O. Rodriguez-Duarte, N. Joachimowicz, B. Duchêne, E. Tedeschi, M. R. Casu, L. Crocco, and F. Vipiana, A Prototype Microwave System for 3D Brain Stroke Imaging, Sensors **20**, 1–16 (2020).

10 R. J. N. Eleutério, *Microwave Imaging of the Axilla to Aid Breast Cancer Diagnosis*, Master's dissertation, Faculdade de Ciências e Tecnologia, Universidade Nova de Lisboa, 2014.

11 M. Savazzi, S. Abedi, N. Ištuk, N. Joachimowicz, H. Roussel, E. Porter, M. O'halloran, J. R. Costa, C. A. Fernandes, J. M. Felício, and R. C. Conceição, Development of an anthropomorphic phantom of the axillary region for microwave imaging assessment, Sensors (Switzerland) **20**, 1–20 (2020).

12 D. M. Godinho, J. M. Felício, C. A. Fernandes, and R. C. Conceição, Experimental Evaluation of an Axillary Microwave Imaging System to Aid Breast Cancer Staging, IEEE Journal of Electromagnetics, RF, and Microwaves in Medicine and Biology **(in press)** (2021).

13 M. C. Gosselin, E. Neufeld, H. Moser, E. Huber, S. Farcito, L. Gerber, M. Jedensjo, I. Hilber, F. D. Gennaro, B. Lloyd, E. Cherubini, D. Szczerba, W. Kainz, and N. Kuster, Development of a new generation of high-resolution anatomical models for medical device

evaluation: The Virtual Population 3.0, Physics in Medicine and Biology **59**, 5287–5303 (2014).

[14] COST European Cooperation in Science & Technology, Memorandum of Understanding for the implementation of the COST Action "European network for advancing Electromagnetic hyperthermic medical technologies" (MyWAVE) CA17115, Technical report, Brussels, 2018.

[15] D. O'Loughlin, M. O'Halloran, B. M. Moloney, M. Glavin, E. Jones, and M. A. Elahi, Microwave breast imaging: Clinical advances and remaining challenges, IEEE Transactions on Biomedical Engineering **65**, 2580–2590 (2018).

[16] W. T. Joines, Y. Zhang, C. Li, and R. L. Jirtle, The measured electrical properties of normal and malignant human tissues from 50 to 900 MHz, Medical Physics **21**, 547–550 (1994).

[17] S. Gabriel, R. W. Lau, and C. Gabriel, The dielectric properties of biological tissues: III Parametric models for the dielectric spectrum of tissues, Physics in Medicine and Biology **41**, 2271–2293 (1996).

[18] M. Lazebnik, L. McCartney, D. Popovic, C. B. Watkins, M. J. Lindstrom, J. Harter, S. Sewall, A. Magliocco, J. H. Booske, M. Okoniewski, and S. C. Hagness, A large-scale study of the ultrawideband microwave dielectric properties of normal breast tissue obtained from reduction surgeries, Physics in Medicine and Biology **52**, 2637–3656 (2007).

[19] J. W. Choi, J. Cho, Y. Lee, J. Yim, B. Kang, K. O. Ki, H. J. Woo, J. K. Hee, C. Cheon, H. D. Lee, and Y. Kwon, Microwave detection of metastasized breast cancer cells in the lymph node; potential application for sentinel lymphadenectomy, Breast Cancer Research and Treatment **86**, 107–115 (2004).

[20] T. R. Cameron, M. Okoniewski, and E. C. Fear, A Preliminary Study of the Electrical Properties of Healthy and Diseased Lymph Nodes, in *International Symposium on Antenna Technology and Applied Electromagnetics & the American Electromagnetics Conference (ANTEM-AMEREM)*, pages 1–3, Ottawa, ON, Canada, 2010.

[21] X. Yu, Y. Sun, K. Cai, H. Yu, D. Zhou, D. Lu, and S. X. Xin, Dielectric Properties of Normal and Metastatic Lymph Nodes Ex Vivo From Lung Cancer Surgeries, Bioelectromagnetics **41**, 148–155 (2020).

[22] S. Standring, Blood, lymphoid tissues and haemopoiesis, in *Gray's Anatomy: The Anatomical Basis of Clinical Practice*, pages 68–80, Elsevier Limited, 41st ed. edition, 2016.

[23] A. La Gioia, M. O'Halloran, and E. Porter, Challenges of Post-measurement Histology for the Dielectric Characterisation of Heterogeneous Biological Tissues, Sensors **20**, 3290–3304 (2020).

[24] D. M. Godinho, J. M. Felicio, T. Castela, N. A. Silva, M. L. Orvalho, C. A. Fernandes, and R. C. Conceicao, Extracting Dielectric Properties for MRI-based Phantoms for Axillary Microwave Imaging Device, in *14th European Conference on Antennas and Propagation, EuCAP 2020*, pages 3–6, Copenhagen, Denmark, 2020.

[25] E. Zastrow, S. K. Davis, M. Lazebnik, F. Kelcz, B. D. V. Veen, and S. C. Hagness, Development of anatomically realistic numerical breast phantoms with accurate dielectric properties for modeling microwave interactions with the human breast, IEEE Transactions on Biomedical Engineering **55**, 2792–2800 (2008).

[26] A. H. Tunçay and I. Akduman, Realistic microwave breast models through T1-weighted 3-D MRI data, IEEE Transactions on Biomedical Engineering **62**, 688–698 (2015).

[27] M. Omer and E. C. Fear, Automated 3D method for the construction of flexible and reconfigurable numerical breast models from MRI scans, Medical and Biological Engineering and Computing **56**, 1027–1040 (2018).

[28] M. Lu, X. Xiao, H. Song, G. Liu, H. Lu, and T. Kikkawa, Accurate construction of 3-D numerical breast models with anatomical information through MRI scans, Computers in Biology and Medicine **130**, 104205 (2021).

[29] G. Unal, G. Slabaugh, A. Ess, A. Yezzi, T. Fang, J. Tyan, M. Requardt, R. Krieg, R. Seethamraju, M. Harisinghani, and R. Weissleder, Semi-automatic lymph node segmentation in LN-MRI, in *International Conference on Image Processing*, pages 77–80, Atlanta, GA, USA, 2006, IEEE.

[30] A. Barbu, M. Suehling, X. Xu, D. Liu, S. K. Zhou, and D. Comaniciu, Automatic detection and segmentation of lymph nodes from CT data, IEEE Transactions on Medical Imaging **31**, 240–250 (2012).

[31] R. Ha, P. Chang, J. Karcich, S. Mutasa, R. Fardanesh, R. T. Wynn, M. Z. Liu, and S. Jambawalikar, Axillary Lymph Node Evaluation Utilizing Convolutional Neural Networks Using MRI Dataset, Journal of Digital Imaging **31**, 851–856 (2018).

[32] N. Mori, K. Tsuchiya, D. Sheth, S. Mugikura, K. Takase, U. Katscher, and H. Abe, Diagnostic value of electric properties tomography (EPT) for differentiating benign from malignant breast lesions: comparison with standard dynamic contrast-enhanced MRI, European Radiology **29**, 1778–1786 (2019).

[33] R. Leijsen, C. van den Berg, A. Webb, R. Remis, and S. Mandija, Combining deep learning and 3D contrast source inversion in MR-based electrical properties tomography, NMR in Biomedicine **e4211**, 1–7 (2019).

[34] H. Q. Woodard and D. R. White, The composition of body tissues, The British Journal of Radiology **59**, 1209–1219 (1986).

[35] Z. Yaniv, B. C. Lowekamp, H. J. Johnson, and R. Beare, SimpleITK Image-Analysis Notebooks: a Collaborative Environment for Education and Reproducible Research, Journal of Digital Imaging **31**, 290–303 (2018).

[36] N. J. Tustison and J. C. Gee, N4ITK: Nick's N3 ITK Implementation For MRI Bias Field Correction, InsightJournal **9**, 1–8 (2009).

[37] N. Otsu, A Threshold Selection Method from Gray-Level Histograms, IEEE Transactions on Systems, Man, and Cybernetics **9**, 62–66 (1979).

[38] D. Arthur and S. Vassilvitskii, k-means++: The Advantages of Careful Seeding, in *Proceedings of the eighteenth annual ACM-SIAM symposium on Discrete algorithms*, pages 1027–1035, New Orleans, Louisiana, USA, 2007, Society for Industrial and Applied Mathematics.

[39] Aleksandr Bazhin, Ellipsoid fit python, Available online: https://github.com/aleksandrbazhin/ellipsoid{_}fit{_}python, 2020.

670 40 D. A. Turner, I. J. Anderson, J. C. Mason, and M. G. Cox, An Algorithm for Fitting an
671   Ellipsoid to Data, Technical Report RR9803, National Physical Laboratory, Middlesex,
672   England, 1999.

673 41 D. M. Godinho, J. M. Felício, T. Castela, N. A. Silva, M. L. Orvalho, C. A.
674   Fernandes, and R. C. Conceição, Axillary Region Models Repository for Elec-
675   tromagnetic Applications, Available online: https://github.com/dmgodinho/
676   axillary-region-models-repository, 2021.

677 42 L. W. Thomas, The Chemical Composition of Adipose Tissue of Man and Mice, Q. J.
678   Exp. Physiol. Cogn. Med. Sci. **47**, 179–188 (1962).

679 43 E. Askew, Water, in *Present Knowledge in Nutrition*, edited by E. Ziegler and L. Filer,
680   pages 98–108, ILSI Press, Washington, DC, 1996.

681 44 L. W. Huwe, W. E. Brown, J. C. Hu, and K. A. Athanasiou, Characterization of costal
682   cartilage and its suitability as a cell source for articular cartilage tissue engineering,
683   Journal of tissue engineering and regenerative medicine **12**, 1163–1176 (2018).

Acknowledgements

Conflict of Interest

The authors have no conflicts to disclose.